Vascular abnormalities in heart and brain are associated with cardiovascular and neurological symptoms in a novel mouse model for Williams syndrome

Hamid el Azzouzi[a,1,2], Laurens W.J. Bosman[b,1,2], Lieke Kros[b], Nicole van Vliet[a], Yanto Ridwan[a,c], Stéphanie Dijkhuizen[b], Erika Sabel-Goedknegt[b], Bastian S. Generowicz[b], Manuele Novello[b], Emma Kretschmann[b], Morrisen Snoeren[b], Danique Broere[b], Rocco Caliandro[a], Sebastiaan K.E. Koekkoek[b], Pieter Kruizinga[b], Vera van Dis[d], Haibo Zhou[e], Hui Yang[e], Changyang Zhou[e], Ingrid van der Pluijm[a,f], Jeroen Essers[a,f,g] and Chris I. De Zeeuw[b,h]

[a] Department of Molecular Genetics, Erasmus MC, Rotterdam, The Netherlands
[b] Department of Neuroscience, Erasmus MC, Rotterdam, The Netherlands
[c] Department of Radiology, Erasmus MC, Rotterdam, The Netherlands
[d] Department of Pathology, Erasmus MC, Rotterdam, The Netherlands
[e] Laboratory of Genome Editing and Brain Diseases, Center for Excellence in Brain Science and Intelligence Technology/Institute of Neuroscience, Chinese Academy of Sciences, Shanghai, China
[f] Department of Vascular Surgery, Erasmus MC, Rotterdam, The Netherlands
[g] Department of Radiotherapy, Erasmus MC, Rotterdam, The Netherlands
[h] Netherlands Institute for Neuroscience, Royal Academy of Arts and Sciences, Amsterdam, The Netherlands

[1] These authors contributed equally.
[2] Correspondence to:
Hamid el Azzouzi, PO Box 2040, 3000 CA Rotterdam, The Netherlands, +31-6-24407347. **Email:** h.elazzouzi@erasmusmc.nl, or to Laurens Bosman, PO Box 2040, 3000 CA Rotterdam, The Netherlands, +31-10-7043358. **Email:** l.bosman@erasmusmc.nl

Competing Interest Statement: The authors declare the absence of competing interests.

Keywords: Williams-Beuren syndrome; elastin, vascularization, cardiac function, social behavior.

Abstract

Williams syndrome is a developmental disorder caused by a microdeletion entailing loss of a single copy of 25-27 genes on chromosome 7q11.23. Patients with Williams syndrome suffer from cardiovascular and neuropsychological symptoms. So far, the structural abnormalities of the cardiovascular system in Williams syndrome have been attributed to the loss of a copy of the elastin (*ELN*) gene. In contrast, the neuropsychological consequences of Williams syndrome, including motor deficits, hypersociability and cognitive impairments, have been mainly attributed to altered expression of transcription factors like LIMK1, GTF2I and GTF2IRD1, while the potential secondary impact of altered cerebrovascular function has been largely ignored. To study the relation between the mutation underlying Williams syndrome and vascularization of not only the heart but also that of the brain, we generated a mouse model with a relatively long microdeletion, including the *Ncf1* gene to reduce the confounding impact of hypertension. The affected mice had an elongated and tortuous aorta, but unlike in *Eln* haploinsufficient mice, there were no signs of structural cardiac hypertrophy. Our Williams syndrome mice had similar structural abnormalities in their coronary and brain vessels, showing disorganized extracellular matrices of the vessel walls. Moreover, our mouse model faithfully replicated both cardiovascular and neurological symptoms of Williams syndrome, highlighting that accurate non-invasive evaluation of complex vascular abnormalities is feasible. Altogether, we present evidence for vascular malformations that are similar in heart and brain, suggesting that cardiovascular and neurological symptoms can both by impacted by changes in the vascular structure in patients with Williams syndrome.

Introduction

Williams syndrome, also known as Williams-Beuren syndrome (WBS), is a developmental multisystem disorder caused by the hemizygous microdeletion of 25-27 genes in the Williams-Beuren syndrome critical region (WBSCR) on chromosome 7q11.23 (Ewart et al., 1993; Pérez Jurado et al., 1996; Peoples et al., 2000; Pober, 2010). Some variation in the length of the deletion occurs between patients, while sporadically much shorter or much longer deletions arise, but the deletion always includes at least the elastin (*ELN*) gene (Howald et al., 2006; Fusco et al., 2014; Lugo et al., 2020) (Fig. 1A). The microdeletion leading to Williams syndrome occurs typically de novo, due to nonallelic homologous recombination between the low copy repeats flanking the WBSCR (Bayés et al., 2003; Hobart et al., 2010). In line with the diversity of genes in the WBSCR, patients with Williams syndrome show a wide variety of symptoms, including cardiovascular abnormalities, distinctive facial features, hypersociability, mild to moderate intellectual disability and mild motor deficits (Williams et al., 1961; Beuren et al., 1962; Bellugi et al., 1990; Hoogenraad et al., 2002; Hoogenraad et al., 2004; van der Geest et al., 2004; Gagliardi et al., 2007; van Hagen et al., 2007; Pober, 2010; Kozel et al., 2021).

Cardiovascular abnormalities, to which patients with Williams syndrome are predisposed, are the main cause of morbidity and mortality and occur in 80% of patients (Collins et al., 2010; Parrish et al., 2020; Bozlak et al., 2023). Of these, supravalvular aortic stenosis (SVAS) is the most common, affecting up to 70% of patients (Collins et al., 2010; Parrish et al., 2020; Bozlak et al., 2023). Peripheral pulmonary artery stenosis (PAS), and to a lesser extent also coarctation of the aorta, ventricular septal defect, patent ductus arteriosus, subaortic stenosis, and hypertrophic cardiomyopathy are also observed in Williams syndrome (Collins et al., 2010; Bozlak et al., 2023).

Patients with mutations restricted to the *ELN* gene can show similar cardiovascular abnormalities, but without the distinctive facial features observed in Williams syndrome (Tassabehji et al., 1999; Urbán et al., 2000; Terashita et al., 2019; Zhou et al., 2022), suggesting that *ELN* hemizygosity is the most important determinant for vascular abnormalities in Williams syndrome. *ELN* encodes tropoelastin that is mainly produced by vascular smooth muscle cells (Belknap et al., 1996). During development, multiple isoforms of tropoelastin are generated via alternative splicing, secreted into the extracellular matrix and

extensively cross-linked to form a network of elastin (Belknap et al., 1996). This imparts elastic properties to the aorta and other arteries, and facilitates the propulsion of blood (Cocciolone et al., 2018).

Like the coronary arteries and the aorta, blood vessels in the brain also have abnormal shapes in patients with Williams syndrome and can develop stenoses (Williams et al., 1961; Wollack et al., 1996; Wint et al., 2014). Although rare, this can predispose patients to develop Moyamoya syndrome (Kawai et al., 1993; Akimoto et al., 2022; Brar et al., 2022), in which stenoses of the large intracranial arteries are accompanied by an increase in small vessels, as well a higher risk of developing hemorrhage (Fukui, 1997; Currie et al., 2011). So far, neurological and psychological consequences of the WBSCR mutation, like hypersociability and cognitive impairments, have been mainly attributed to the altered expression of the transcription factors LIMK1, GTF2I and GTF2IRD1 (Borralleras et al., 2015; Kozel et al., 2021) and structural proteins like CLIP-115 (Hoogenraad et al., 1998; Hoogenraad et al., 2002; Hoogenraad et al., 2004; van der Geest et al., 2004; van Hagen et al., 2007), while the impact of altered cerebrovascular function has largely been ignored.

To study the relation between the WBSCR mutation and the shape and constitution of the aorta and the blood vessels of both heart and brain, we generated a mouse model with a longer microdeletion than in previous models (Li et al., 2009; Segura-Puimedon et al., 2014). The main difference between our mouse model and a previously published model (Segura-Puimedon et al., 2014), is that our microdeletion includes also the *Ncf1* gene that codes for neutrophil cytosolic factor 1. In patients, inclusion of *NCF1* in the deleted region has been suggested to reduce the risk of hypertension to which other patients with Williams syndrome are predisposed (Del Campo et al., 2006). Thus, our mouse model mimics the human situation in the absence of a genetic cause for hypertension, which makes the interpretation of the vascular deficits less complicated. The model faithfully recapitulates the spectrum of symptoms of patients, involving cardiovascular, craniofacial and neurological abnormalities. Our mouse model is, therefore, valuable for understanding the anatomical, molecular and functional impact of the microdeletion leading to Williams syndrome.

Results

Generation and validation of a novel mouse model for Williams syndrome

In order to obtain a mouse model with a longer microdeletion than used previously (Li et al., 2009; Segura-Puimedon et al., 2014), we employed CRISPR/Cas9-mediated excision to successfully create a viable mouse line (Fig. 1A-B). Male, in contrast to female, $WBS^{+/-}$ mice showed a mildly reduced body weight (Fig. S1).

To validate our new mouse model, we first characterized its anatomical and behavioral phenotypes, and compared these to symptoms observed in patients with Williams syndrome as well as with the previously published mouse models (Table S1). Patients with Williams syndrome display characteristic facial features (Williams et al., 1961; Hammond et al., 2005; Liu et al., 2021), and the previously published complete deletion (CD) mouse model has smaller skulls with reduced mandibles (Segura-Puimedon et al., 2014). Micro-computed tomography (µCT) revealed that also our mice show cranial aberrations, in particular a shorter nasal bone and a flattened parietal bone (Fig. 1C, S2).

We subsequently subjected our mice to a battery of behavioral tests, starting with a general test for muscle strength, the hanging wire test. This did not reveal any marked differences between our $WBS^{+/-}$ mice and their wild-type littermates (Fig. 1D).

Next, we tested the mice on the balance beam, as patients have mild balance problems (Barozzi et al., 2013). We found similar crossing times and number of hindlimb slips in mutant and control mice. However, our $WBS^{+/-}$ mice showed an increased tendency to crawl rather than to walk across the beam (Fig. S3), which might be a compensatory mechanism for reduced balance. Overall, we have to conclude that there were not more than subtle differences in behavior on the balance beam, and we investigated the locomotor phenotype further on the ErasmusLadder, which consists of a horizontal ladder with alternating lower and higher rungs between two shelter boxes (Fig.

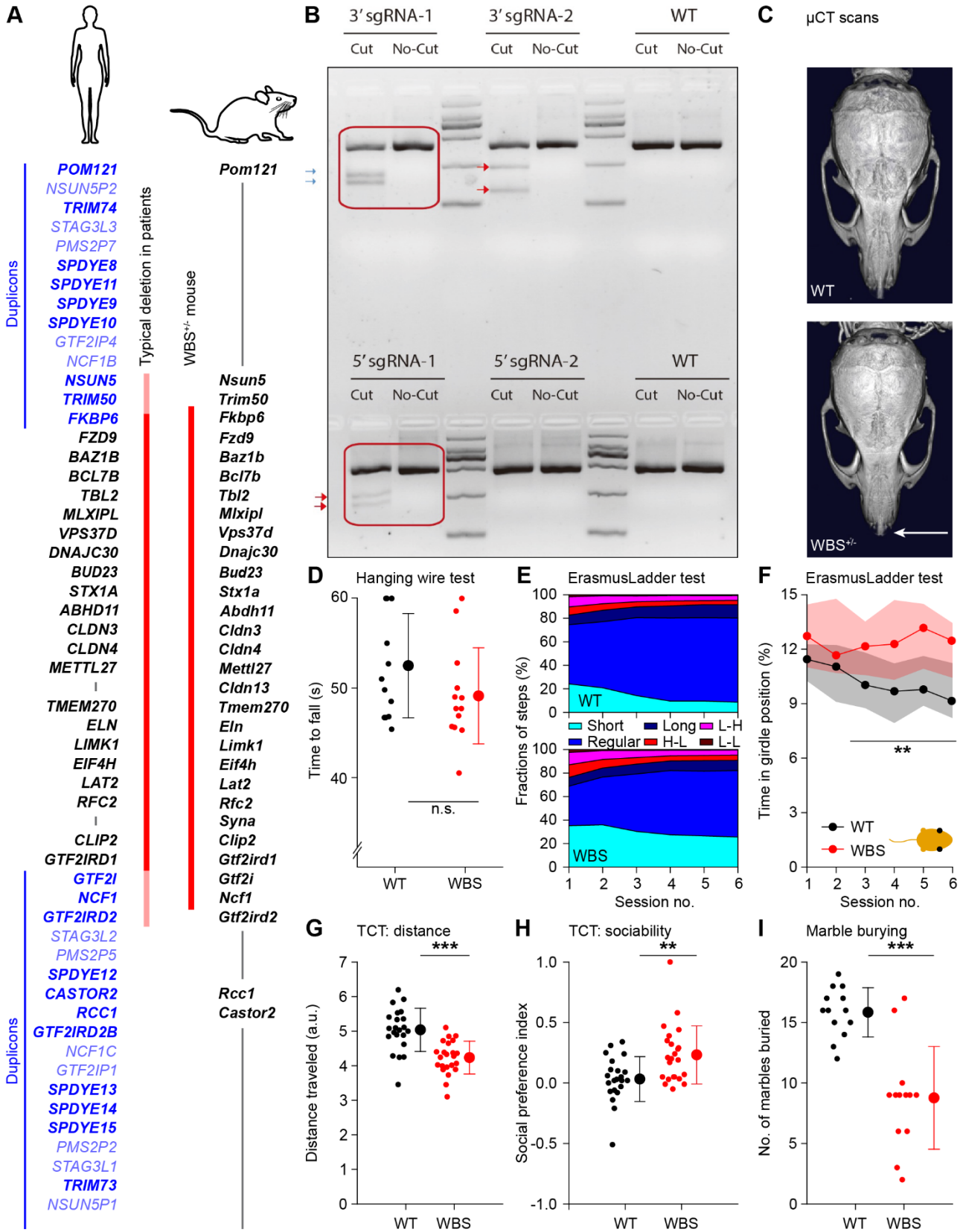
A
Duplicons
POM121
NSUN5P2
TRIM74
STAG3L3
PMS2P7
SPDYE8
SPDYE11
SPDYE9
SPDYE10
GTF2IP4
NCF1B
NSUN5
TRIM50
FKBP6
FZD9
BAZ1B
BCL7B
TBL2
MLXIPL
VPS37D
DNAJC30
BUD23
STX1A
ABHD11
CLDN3
CLDN4
METTL27
TMEM270
ELN
LIMK1
EIF4H
LAT2
RFC2
CLIP2
GTF2IRD1
GTF2I
NCF1
GTF2IRD2
STAG3L2
PMS2P5
SPDYE12
CASTOR2
RCC1
GTF2IRD2B
NCF1C
GTF2IP1
SPDYE13
SPDYE14
SPDYE15
PMS2P2
STAG3L1
TRIM73
NSUN5P1
Typical deletion in patients
WBS+/- mouse
Pom121
Nsun5
Trim50
Fkbp6
Fzd9
Baz1b
Bcl7b
Tbl2
Mlxipl
Vps37d
Dnajc30
Bud23
Stx1a
Abdh11
Cldn3
Cldn4
Mettl27
Cldn13
Tmem270
Eln
Limk1
Eif4h
Lat2
Rfc2
Syna
Clip2
Gtf2ird1
Gtf2i
Ncf1
Gtf2ird2
Rcc1
Castor2
B
3′ sgRNA-1
3′ sgRNA-2
WT
Cut
No-Cut
5′ sgRNA-1
5′ sgRNA-2
C
µCT scans
WT
WBS+/-
D
Hanging wire test
Time to fall (s)
n.s.
E
ErasmusLadder test
Fractions of steps (%)
Short
Long
L-H
Regular
H-L
L-L
Session no.
F
ErasmusLadder test
Time in girdle position (%)
**
Session no.
G
TCT: distance
***
Distance traveled (a.u.)
H
TCT: sociability
**
Social preference index
I
Marble burying
***
No. of marbles buried

Figure 1. Creation and validation of a mouse model for Williams syndrome.
(A) On human chromosome 7, the Williams-Beuren critical region (WBSCR) is flanked by two duplicons. In these duplicons, several pseudogenes (light blue) occur that do not code for proteins but that are duplicates of coding genes. Misalignment during meiosis can result in a microdeletion within this area. The exact locations of the breach can vary between patients, but the large majority of patients have a microdeletion of 25-27 genes (red line, the light red regions indicate areas that are sometimes included and sometimes not). In mice, a homologous region can be found on chromosome 5. The red line on the right indicates the genes hemizygously absent in our $WBS^{+/-}$ mouse model. *(B)* Blots, highlighting the specificity of our mouse model. All genes in between *Trim50* and *Gtf2ird2* on chromosome 5 were deleted with CRISPR/Cas9 technology. Two cuts were performed on each side in the chromosome region of interest, and filaments of single-stranded oligodeoxyribonucleotide (ssODN) (100nt) were inserted on each side of the region of the deleted gene to attach the two free extremities of each cut region. A T7 endonuclease 1 (T7E1) mismatch detection assay was used to evaluate the cut efficiency and the activity of site-specific nucleases. *(C)* $WBS^{+/-}$ mice have a more compact skull than their WT littermates, which is especially evident from the shorter nasal bone (see also Fig. S2). Reconstructions made from µCT scans. *(D)* WT and $WBS^{+/-}$ mice had similar performance on the hanging wire test (p = 0.138; for details on statistics of the behavioral analysis represented in this Figure, see Table S2). *(E)* On the ErasmusLadder test, $WBS^{+/-}$ mice made relatively many short steps (steps from one higher rung to the next one, skipping the lower rung in between) at the expense of regular steps (steps from one higher rung to the over-next one, skipping one higher rung and two lower rungs). The difference between regular and short steps was statistically significant (p = 0.005). *(F)* The fraction of the step cycle during which mice use their two front limbs as support is larger in $WBS^{+/-}$ mice than in wild-type littermates (p < 0.01). *(G)* During the first phase of the three-chamber test (see Fig. S6A), $WBS^{+/-}$ mice traveled less than their WT littermates (p <0.001). *(H)* During the second phase of the test, $WBS^{+/-}$ mice showed higher sociability than their WT littermates (p = 0.003). *(I)* Mice were placed in a cage with 20 equally spaced marbles and the numbers of marbles buried within 30 minutes were counted (p <0.001).

S4A). Sensory cues guide the timing of trial starts, and in general, $WBS^{+/-}$ and control mice showed a similar tendency to wait for the second sensory cue to start a trial. On the last day of training, however, $WBS^{+/-}$ mice tried to enter the ladder more often before trial start than did their control littermates (Fig. S4B-C).

Once on the ladder, $WBS^{+/-}$ mice did not show a clear decrease in speed or regularity of step timing, nor a notable increase in lower rung touches, but they did make shorter steps than their wild-type littermates (Fig. 1E,F, S4D-J). The latter phenomenon is also observed in patients (Ito et al., 2020). Remarkably, the variation in step size was very large between individual $WBS^{+/-}$ mice, with roughly half the mice making as few short steps as the wild-type mice (Fig. S4I). Thus, this initial analysis revealed only a relatively mild, yet present, gaiting deficit in $WBS^{+/-}$ mice.

A further examination of the inter-limb coordination, revealed that $WBS^{+/-}$ mice more often than WT mice touch the rungs with both front limbs simultaneously (Fig. 1F, Fig. S4K). Using Hildebrand plots (Hildebrand, 1965; Jaarsma et al., 2023) in combination with unsupervised machine learning revealed that the coordination between the limbs was mildly affected in $WBS^{+/-}$ mice (Fig. S5). Thus, overall, $WBS^{+/-}$ mice have a mild locomotor phenotype (Fig. S4L).

Next, we examined social behavior in $WBS^{+/-}$ mice, as patients with Williams syndrome are well known for their lack of stranger awareness, often termed as hypersociability (Tomc et al., 1990; Doyle et al., 2004; Meyer-Lindenberg et al., 2005). Other mouse models for Williams syndrome also showed increased interest in other mice (Li et al., 2009; Segura-Puimedon et al., 2014; Kopp et al., 2019; Ortiz-Romero et al., 2021). To characterize social behavior in our mouse line, we observed their behavior in the three-chamber test. We performed this test in three phases (Fig. S6A). During the first phase, mice were allowed to explore the test environment for 10 min. During this phase, no other mice were present. Although the $WBS^{+/-}$ mice

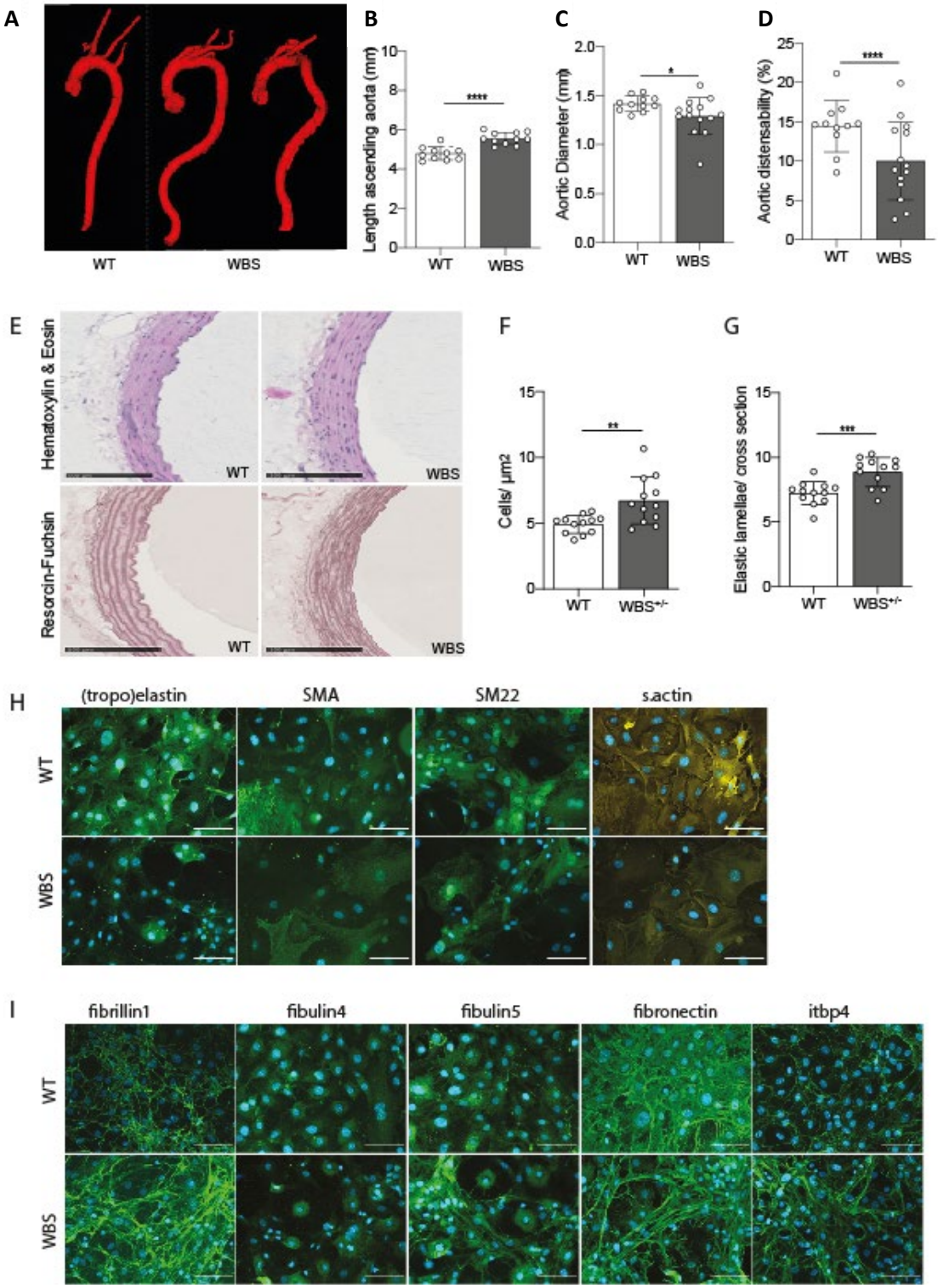
A
WT
WBS
B
Length ascending aorta (mm)
****
WT
WBS
C
Aortic Diameter (mm)
*
WT
WBS
D
Aortic distensability (%)
****
WT
WBS
E
Hematoxylin & Eosin
Resorcin-Fuchsin
WT
WBS
F
Cells/ µm2
**
WT
WBS+/-
G
Elastic lamellae/ cross section
***
WT
WBS+/-
H
(tropo)elastin
SMA
SM22
s.actin
WT
WBS
I
fibrillin1
fibulin4
fibulin5
fibronectin
itbp4
WT
WBS

Figure 2. Vascular extracellular matrix abnormalities in WBS$^{+/-}$ mice.
(A) Examples of 3D rendering of the aortas of wild-type and WBS$^{+/-}$ mice. *(B, C)* The aortae of WBS$^{+/-}$ mice are elongated and have a narrower lumen. *(D)* A lower distensibility (expansion of the aorta during systole) was found in aortas of WBS$^{+/-}$ mice. *(E)* Examples of hematoxylin-eosin and resorcin-fuchsin staining of cross-sections from wild-type and WBS$^{+/-}$ mice. *(F)* Cell density measurements on aortic cross sections, defined as the number of cells per mm^2, showed an increase in cells in the aortas of WBS$^{+/-}$ mice. *(G)* Quantification of the resorcin-fuchsin staining for the elastic lamellae present in the aortic wall, shows more, but less organized elastin sheets in the medial layers of the aorta wall of WBS$^{+/-}$ mice. *(H)* Normal immunofluorescent staining of smooth muscle cells isolated from the aortic arch for smooth muscle actin (SMA) and smooth muscle 22 (SM22). In contrast, tropoelastin and sir-actin were decreased in WBS$^{+/-}$ mice. *(I)* Vascular smooth muscle cells from WBS$^{+/-}$ mice showed an increase in fibrilin1, and reduced levels of fibulin4 and fibronectin. The levels of fibulin5 and Itbp4 were unchanged. Magnification 20x, scale bar 100 µm. *$p < 0.05$; **$p < 0.01$, ***$p < 0.005$, error bars show s.e.m..

traveled less during this phase (WT: 5.0 ± 0.6 a.u.; WBS$^{+/-}$: 4.2 ± 4.7 a.u.; p <0.001, t = 4.857, t test, n = 22 WT and 23 WBS$^{+/-}$ mice; Fig. 1G), they did spend equal amounts of time in each of the three chambers, as the WT mice did (Fig. S6B). During the second phase, another mouse was present in a wire mash cup within one of the two outer chambers whereas an empty cup was placed in the other. Like wild-type mice, WBS$^{+/-}$ mice spent more time in the chamber with the other mouse than in the opposite chamber, but the WBS$^{+/-}$ mice showed a stronger bias toward the social chamber than did their wild-type littermates (p = 0.003, t = 3.135, t test; Fig. 1H and *Fig. S6B*). Finally, during the third phase, the chamber opposite to the chamber with the other mouse contained yet another mouse. The novel mouse, however, did not attract more attention from WBS$^{+/-}$ mice than from wild-type mice (p = 0.748, t = 0.324, t test; Fig. S6B). Thus, WBS$^{+/-}$ mice showed a larger social preference than their wild-type littermates, which confirms their hypersocial phenotype.

Finally, we tested obsessive-compulsive behavior using the marble burying test and found that WBS$^{+/-}$ mice buried significantly less marbles in 30 minutes than their wild-type littermates (WT: 16 (2) marbles buried; WBS$^{+/-}$: 9 (3); medians (inter-quartile range, IQR); p <0.001, U = 15.5, Mann-Whitney test, n = 13 mice/genotype; Fig. 1I, Fig. S6C). Overall, we conclude that our novel mouse model recapitulates key facial and neurological symptoms observed in patients.

Abnormal morphology of the aorta

Since many patients with Williams syndrome have been shown to present with aortic abnormalities (Collins et al., 2010; Parrish et al., 2020; Bozlak et al., 2023), we studied the 3D morphology of the aortas using µCT. WBS$^{+/-}$ mice have more dilated aortic roots and longer ascending aortas than their wild-type littermates (Fig. 2A-B). In addition, ultrasound imaging indicated that WBS$^{+/-}$ mice also show narrowing of the aortic lumen and a reduction of the aortic elasticity (Fig. 2C-D). In WBS$^{+/-}$ mice, the wall of the ascending aorta contained more cells and more elastic lamellae than in wild-type littermates (Fig. 2E-G). However, these elastic lamellae were disrupted and less organized than in wild-type littermates (Fig. 2E).

Subsequently, we further characterized the structure of the aortic wall by analyzing the extracellular matrix of vascular smooth muscle cells. To this end, we cultured smooth muscle cells that were isolated from the aortic wall. Despite a reduction in the production of tropoelastin, in line with the haploinsufficiency of *Eln*, expression of smooth muscle-specific markers, i.e., Smooth Muscle Actin (SMA) and Smooth Muscle 22 (SM22), were similar between cell lines derived from WBS$^{+/-}$ mice and wild-type littermates (Fig. 2H). Considering that elastin is associated with fibrillin-1 (FBN-1) to form the elastic microfibrils in the extracellular matrix (Thomson et al., 2019), we also investigated FBN-1 expression in both cell lines. Mutant vascular smooth muscle cells revealed an increase in FBN-1 production (Fig. 2I). However, although the FBN-1 fibers were thicker, they were more disorganized with respect to cells from wild-type mice, in line with the situation in vivo (Fig.

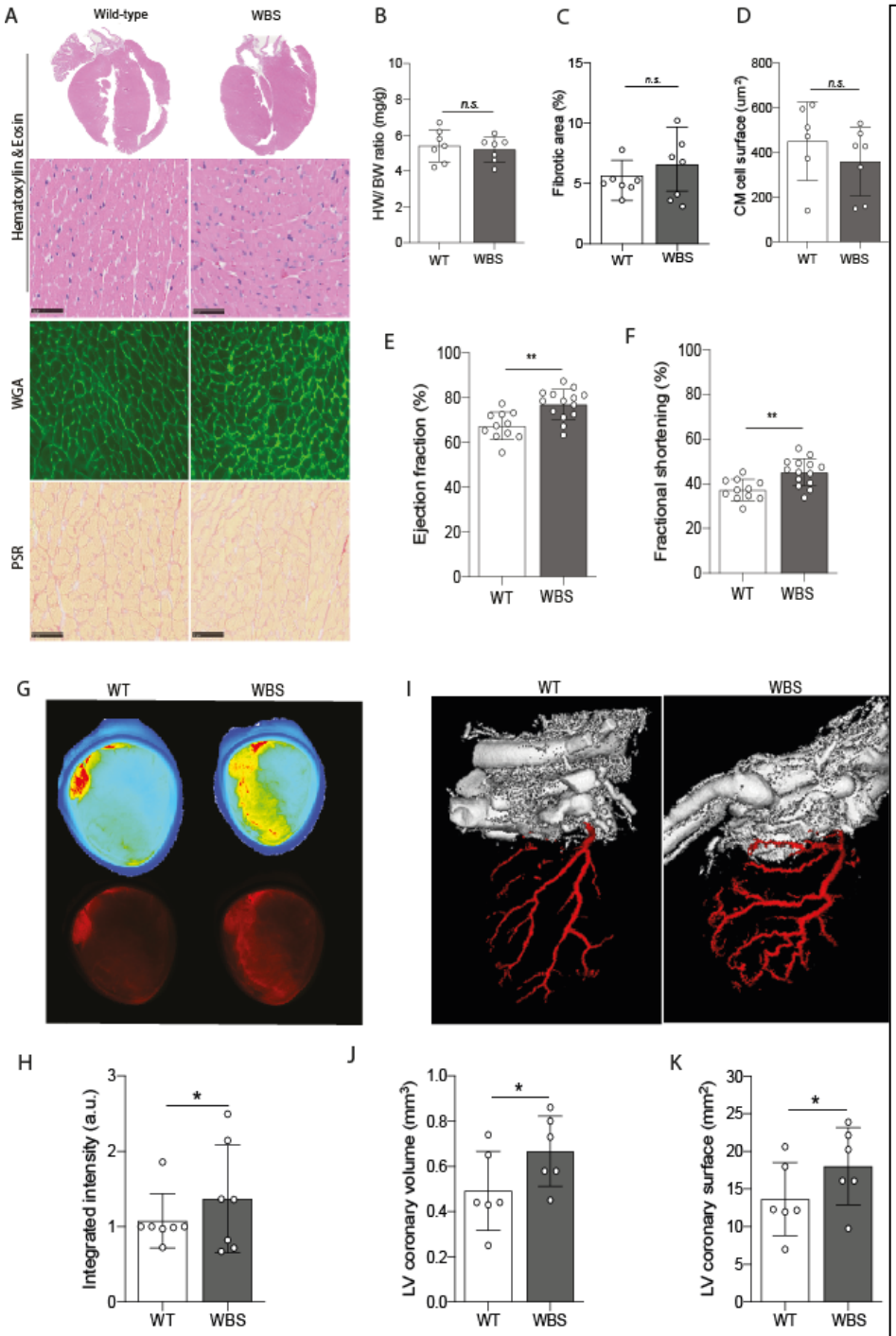

2E). Next, we analyzed Fibulin-4 and Fibulin-5 which form a class of extracellular matrix proteins tightly linked to the elastic microfibrils, but we did not find marked differences in expression of these proteins (Fig. 2I). Finally, we focused on fibronectin (FN), which is another filamentous protein present in the extracellular matrix. FN turned out to be less expressed

Figure 3. Relatively normal cardiac morphology and function of WBS$^{+/-}$ mice despite coronary anomalies. *(A)* Representative examples of whole hearts (top panels), H&E-stained (middle panels), WGA labeled (middle panels) and Picroserious (PSR)-stained (lower panels) sections from wild-type and WBS$^{+/-}$ mice. *(B)* Gravimetric analysis of corrected heart weights in wild-type and WBS$^{+/-}$ mice. *(C)* Analysis of cardiomyocyte hypertrophy in cardiac tissue sections. Slices (6 µm) of the left ventricular myocardium were stained with Alexa 647–labeled WGA for determination of myocyte cross-sectional areas. *(D)* Quantification of collagen density in cardiac tissue sections. Transthoracic echocardiography analysis with *(E)* quantification of ejection fraction (EF) and *(F)* fractional shortening (FS), showing an increased in the WBS$^{+/-}$ mouse hearts. *(G)* Representative examples of the NIRF probe MMPSense 680 in ex vivo hearts. *(H)* Quantification of MMP activity in hearts shows increased matrix remodeling in cardiac coronaries of WBS$^{+/-}$ mice. *(I)* 3D rendering of the coronaries using microfil blood vessel casting and µCT imaging. *(J)* Quantification of total left ventricle coronary volume in mm^3. *(K)* Quantification of total left ventricle coronary surface area in mm^2. *p < 0.05; **p < 0.01, ***p < 0.005, error bars represent s.e.m.

by vascular smooth muscle cells (Fig. 2I). Moreover, the overall structure of the FN scaffold was shown to be less dense and poorly organized compared with the fiber formation found in the control cell line.

Thus, the aortas of $WBS^{+/-}$ mice show the same morphological changes as found in patients, and these are associated with alterations in the composition of the aortic wall, in particular an increase in smooth muscle cells and a lack of organization in the elastic lamellae, as shown both in post mortem tissue as well as in cell cultures of vascular smooth muscle cells.

Normal cardiac morphology

Comparable to $WBS^{+/-}$ mice, mice that are haploinsufficient for only the *Eln* gene ($Eln^{+/-}$ mice) have morphological changes of their aortic walls, and these are associated with hypertension and cardiac hypertrophy (Hawes et al., 2020). In contrast, $WBS^{+/-}$ mice do not display abnormal heart weight upon autopsy, nor was the FITC-labeled wheat-germ-agglutinin (WGA) staining, indicative of a hypertrophic response, significantly different in hearts of $WBS^{+/-}$ mice. Accordingly, hearts of $WBS^{+/-}$ mice did not show any myocyte disarray or significant differences of interstitial fibrosis (Fig. 3A-D). Despite normal cardiac morphology, echocardiography revealed an increased ejection fraction, indicating a larger cardiac contractility, in $WBS^{+/-}$ than in wild-type mice (Fig. 3E). Similarly, the fractional shortening was also increased in $WBS^{+/-}$ mice (Fig. 3F). Overall, the hearts of $WBS^{+/-}$ mice appeared anatomically relatively normal, but their abnormal functioning was in line with a higher resistance of the aorta.

Coronary artery abnormalities

Patients with Williams syndrome, similar to those suffering from congenital supravalvular aortic stenosis, often experience the consequences of coronary artery abnormalities (Parrish et al., 2020). The latter may manifest as coronary ostial stenosis, diffuse coronary artery stenosis, coronary artery dilation, or obstruction of coronary artery inflow by the aortic valves (Tonelli et al., 2015). As arterial malfunction is often linked to remodeling of the extracellular matrix, we measured the activity of matrix metalloproteinases (MMPs) that are responsible for extracellular matrix degradation. MMPs are a family of latent zinc- and calcium-dependent enzymes, and they are involved in the pathogenesis of many diseases, such as atherosclerosis, cardiomyopathies, rheumatoid arthritis, neuroinflammatory diseases and stroke (Hutchinson et al., 2010; Wågsäter et al., 2011; Brkic et al., 2015; Bräuninger et al., 2023). Using MMPSense 680, a fluorescent probe activated by matrix metalloproteinases, we found increased MMP activity in the coronary arteries of $WBS^{+/-}$ mice, but not in the aorta (Fig. 3G-H). To quantify whether these changes in the extracellular matrix were associated with altered morphology, we visualized the cardiac coronary vascular system using microfil-perfusion in combination with µCT (Fig. 3I-K). Thus, $WBS^{+/-}$ mice display increased MMP activity in their coronary arteries, which can be associated with longer and more tortuous coronaries commonly observed in patients (Pober et al., 2008).

Alterations in cerebral vasculature

In contrast to aortic and coronary pathology, vascular abnormalities in the brain have so far received relatively little attention. Yet, case reports have documented that cerebral vessels can also be tortuous and stenotic in patients with Williams syndrome (Williams et al., 1961; Soper et al., 1995; Wint et al., 2014). To examine putative aberrations in the cerebral vasculature in $WBS^{+/-}$ mice, we first used post mortem µCT to characterize the circle of Willis and related large vessels. Indeed, these large vessels displayed increased tortuosity in $WBS^{+/-}$ mice (Fig. 4A, Fig. S7). As the spatial resolution of µCT is limited, we subsequently used in vivo micro-Doppler imaging to additionally visualize smaller vessels. These scans confirmed what we already noticed on the µCT images, showing tortuous vascularization (Fig. 4B, S8).

To study whether also the microvasculature was affected by the WBSCR mutation, we perfused mice with ink to visualize all blood vessels, and made 50 µm thick tissue slices (Fig. 4C, S9). In a first attempt to identify putative changes in micro-vascularization, we calculated the fractal dimensions of skeletonized images and found that these were similar for both genotypes (WT (n = 7): 1.55 (0.04), $WBS^{+/-}$ (n = 9): 1.58 (0.06), medians (inter-quartile range), $p = 0.470$, Mann-Whitney test). Additionally, the tortuosity of the small vessels turned out to be very comparable between

both genotypes (WT (n = 8): 1.04 (0.01), $WBS^{+/-}$ (n = 9): 1.04 (0.00), median (inter-quartile ranges), p = 0.171, Mann-Whitney test). However, we found that irregular structures, like stubs, right-angled curves and spirals, were more abundant than in $WBS^{+/-}$ than in wild-type mice (Fig. 4D, S10). We quantified the occurrence of spirals in fragments of the cerebellum, hippocampus and brainstem, and found them to be significantly more abundant in $WBS^{+/-}$ mice (WT: 4.5 ± 2.9 loops, $WBS^{+/-}$: 7.4 ± 4.9 loops, means ± s.d., p = 0.010, t test, Fig. 4E). Thus, we conclude that the large vessels of the brain, which normally contain a high level of elastin, are clearly affected in $WBS^{+/-}$ mice, similar to the aorta and coronary arteries. In contrast, the smaller vessels appear generally normal, but a significant, yet relatively small, fraction of these vessels show abnormal appearances.

Discussion

In this study, we focused on the vascular aspects of Williams syndrome that may not only affect the cardiovascular system, but also the central nervous system. Previously, mouse models have underscored the prominent role of the elastic matrix in the morphogenesis and homeostasis of the vascular wall (Dietz and Mecham, 2000). For example, a fibulin-5 KO mouse model has been used to show that defective organization and stabilization of elastic fibers produces stiffer arteries (Yanagisawa et al., 2009). Moreover, fibulin-2 and fibulin-5, which direct the assembly of elastic fibers and thereby the internal elastic lamina during postnatal development through, are responsible for maintenance of the adult vessel wall (Chapman et al., 2010). Here, we created a new mouse model for Williams syndrome, with a mutation of a large set of 26 genes, mimicking that shown in patients. Patients with Williams syndrome may be especially vulnerable to develop hypertension when their mutation spares the *NCF1* gene (Del Campo et al., 2006), as is the case in the previously published CD mouse model (Segura-Puimedon et al., 2014). Instead, in our mouse model, *NCF1* is included in the microdeletion, and this model indeed shows no signs of hypertrophy of the walls of the cardiac ventricles. This stands in marked contrast not only to the phenotype of the CD mouse model (Segura-Puimedon et al., 2014), but also to that of *ELN* haploinsufficiency (Hawes et al., 2020). Together, these data highlight the potential interactions of genes within the WBSCR, even when only considering the cardiovascular system. Moreover, we also show here for the first time that the micro-vascularization of the brain may be affected in Williams syndrome, indicating that genes of the WBSCR may also well interact in terms of affecting the neuropsychological symptoms via a primary vascular defect in the CNS. For example, the cerebrovascular aberrations may potentially lead to hypoperfusion and hypoxia in particular brain regions during neural development, and thereby elicit particular cognitive and behavioral features, including cognitive weaknesses and social limitations. Thus, to fully understand the pathological mechanisms of Williams syndrome, it appears relevant to not only study knock outs of single genes or a limited set of genes, but also to generate and investigate mouse models that comprise heterozygous deletions of most, if not all, of the genes implicated in Williams syndrome.

In a first general screening, we characterized a number of characteristic features of Williams syndrome, including reduced body size, craniofacial peculiarities, abnormal gait and hypersociability (Fig. 1). Overall, our mouse model demonstrated to be a faithful representation of the human condition. It was interesting to note, however, that the gait problems we observed were not typical for cerebellar ataxia (Vinueza Veloz et al., 2015; Jaarsma et al., 2023), suggesting implication of non-cerebellar regions underlying the motor phenotype.

Next, we conducted morphological and morphometrical analysis of the cardiovascular phenotype of $WBS^{+/-}$ mice and their wild-type littermates, and demonstrated that $WBS^{+/-}$ mice harbor abnormalities in the cardiocirculatory system. $WBS^{+/-}$ mice have a longer and more tortuous aorta with an overall narrowing of the aortic lumen and a reduction of elasticity compared to wild-type mice. Moreover, the ascending part of the aorta was longer and contained a more dilated aortic root in $WBS^{+/-}$ mice indicating a phenotypic comparison to aortas of patients. In addition, we observed alterations in the activity of metalloproteinases (MMP2, MMP9, MMP7) in $WBS^{+/-}$ mice, hinting towards decreased level of MMPs activation compared to wild-type littermates.

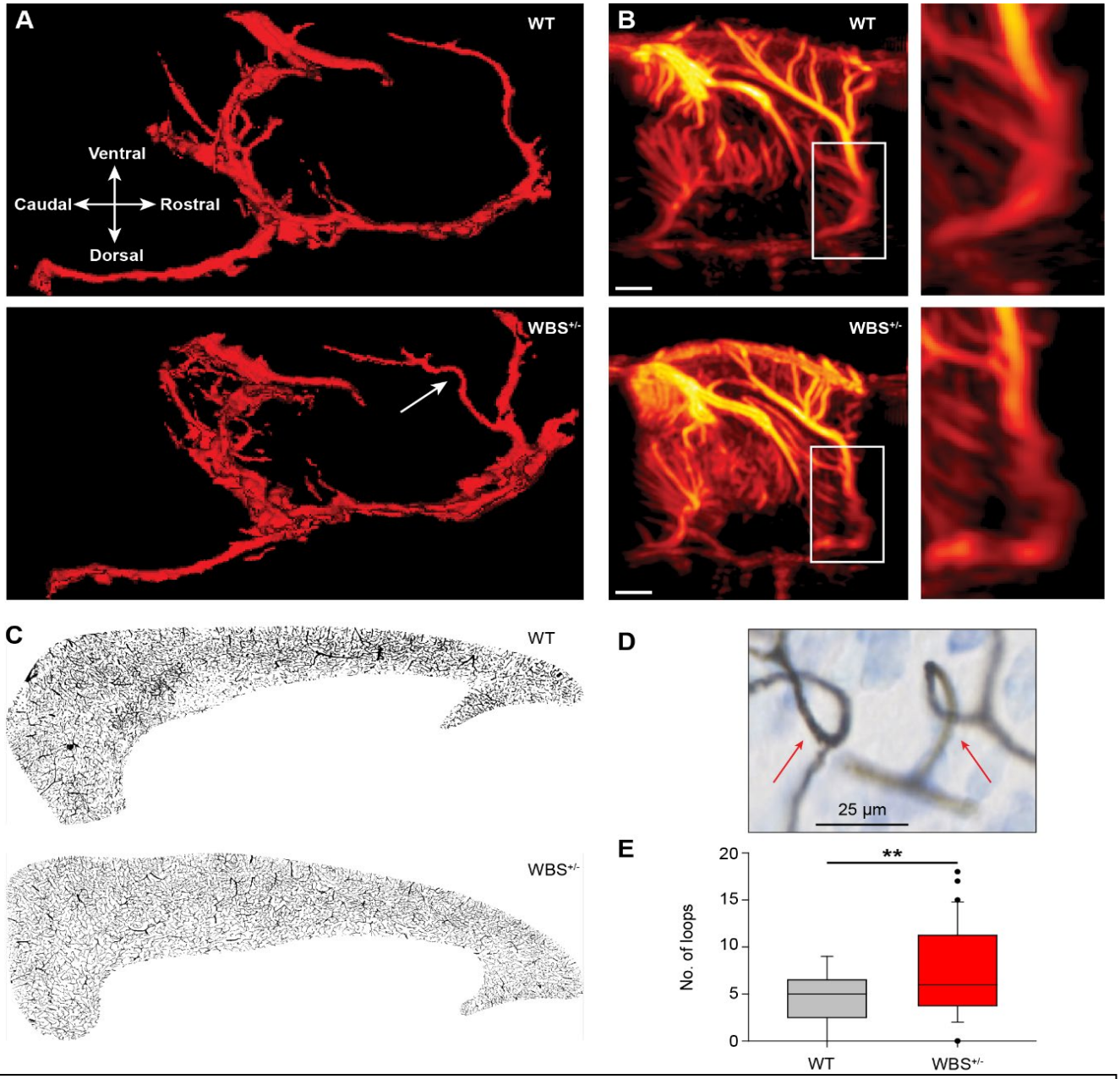

Figure 4. **Abnormal vasculature in the brain.**
(A) Representative example of the largest blood vessels in the brain, using post mortem µCT. *(B)* As in A but using in vivo ultrasound imaging. Images on the right show a magnification of the part of the left image indicated by the rectangles. *(C)* Examples of binarized sagittal sections (50 µm thick) through the cerebral cortex, showing the vascularization. *(D)* Example of loops observed in small vessels. *(E)* Quantification of the number of loops seen in brain slices. An increased number of loops in small vessels was found $WBS^{+/-}$ mice. $^{**}p < 0.01$, error bars represent inter-quartile ranges.

Further analysis showed that the structural abnormalities in aortas of $WBS^{+/-}$ mice, like differences in lamellar units and thickness, are mainly driven by hyperplasia of cells in the medial layer of the aortic wall. In line with the fact that elastin has been shown to be essential for vascular integrity (Cocciolone et al.,

2018), our analysis showed that the elastic lamellae in the aortic wall of the WBS mice are disorganized and fragmented compared to wild-type littermates. Strikingly, other components of the extracellular matrix, such as total collagen deposition, showed no significant differences.

Abnormalities in the cardiocirculatory system are often accompanied with cardiac dysfunction. However, functional analysis of $WBS^{+/-}$ mice did not reveal marked impairments. Hearts of $WBS^{+/-}$ mice did not show any significant structural differences indicating that aortic abnormalities did not cause major hemodynamic or structural differences in hearts of $WBS^{+/-}$ mice. This diverges from the fact that haploinsufficiency of elastin exacerbates cardiac hypertrophy (Hawes et al., 2020), highlighting a potential interaction between elastin and NCF1.

Patients with Williams syndrome show coronary artery malfunction that resembles that following congenital supravalvular aortic stenosis. Since MMP-dependent extracellular matrix remodeling is a major determinant of artery function (Hutchinson et al., 2010; Wågsäter et al., 2011; Brkic et al., 2015; Bräuninger et al., 2023), we analyzed MMP activity in the coronary arteries and found increased activity in the hearts of $WBS^{+/-}$ mice. Moreover, perfusion casting showed abnormalities in the coronary macro-vasculature of $WBS^{+/-}$ mice that are consistent with longer and more tortuous coronary arteries, akin the situation in patients where dilated and tortuous coronary arteries are commonly seen. In line with the important role of vascular smooth muscle cells in the production of extracellular matrix, $WBS^{+/-}$ mice produce less elastin, and if they do, with poorly organized microfibrils. This indicates that haploinsufficiency for *Eln* is the main key for a disorganized extracellular matrix.

Investigation of the cerebral vessels revealed that they displayed similar malformations as found in the aorta and the coronary arteries. Aberrant vascularization in the brain of $WBS^{+/-}$ mice was present at all levels, from excessive branching of the smallest vessels until tortuosity in the large vessels that are associated to the circle of Willis. Taken together, these data indicate that aberrant extracellular matrix remodeling due to lack of elastin also contributes to the vascular phenotype seen in WBS. We hypothesize that the altered morphology of the cerebral blood vessels may contribute to the neuropsychological symptoms of Williams syndrome. Thus, this would be an additional factor that can modulate neural function next to the known impact of the transcription factors LIMK1, CYLN2, GTF2I and GTF2IRD1, as well as other genes in the WBSCR (Hoogenraad et al., 1998; Hoogenraad et al., 2002; Hoogenraad et al., 2004; van der Geest et al., 2004; van Hagen et al., 2007; Borralleras et al., 2015; Kozel et al., 2021).

Materials and Methods

Ethics Statements

Animals were generated and the experiments were performed at the Chinese Academy of Science (CAS) according to institutional guidelines as overseen by Animal Welfare Board of the CAS, following Chinese legislation, as well as at the Erasmus MC, following Dutch and EU legislation. Prior to the start of the experiments, project licenses for the animal experiments performed for this study at the Erasmus MC was obtained from the Dutch national authority and filed under no. AVD101002015273 and AVD1010020197846.

Generation of $WBS^{+/-}$ mouse model

To generate the $WBS^{+/-}$ mouse model, we used CRISPR/Cas9 technology (Leonova and Gainetdinov, 2020) to delete the genes between *Trim50* and *Gtf2ird2* on chromosome 5. The genes within this region correspond to the analogous region on chromosome 7q11.23 in humans (DeSilva et al., 2002), whose heterozygous deletion leads to the development of Williams syndrome. CRISPR/Cas9 technology modifies the site-specific locations of the selected genes, leading to deletions of this region. 2 cuts have been performed on each side in our chromosome region of interest. The knockout fragment equals 1.1 M. After cutting, filaments of single-stranded oligodeoxyribonucleotide (ssODN) (100nt) were inserted on each side of the region of the deleted gene to attach the two free extremities of each cut region. The sequences of the single guide RNA (sgRNA) are: 5′ sgRNA-1 is agggccacacccatggctgc; for 5′ sgRNA-2 is ctgagtgcacatatagtgct; sgRNA-1 is tcccaaggtcatccagaatc; 3′ sgRNA-2 is

ggtcacacaccacgagactg. After that, a T7 endonuclease 1 (T7E1) mismatch detection assay was performed to evaluate the cut efficiency or the activity of site-specific nucleases (Sentmanat et al., 2018), and this revealed a high cut efficiency (Fig. 1B). In total, 48 mice were generated and tested for their cutting DNA efficiency. Finally, Sanger sequencing of polymerase chain reaction product (PCR) was performed to confirm the real cutting. The mice had a C57BL/6J background.

Animals were group housed in a general mouse facility. Environment was controlled with a temperature of 20–22°C and 12 h light:12 h dark cycles. Food and water were offered ad libitum. Experiments were performed on groups of mixed sex. Experimenters were blind to the genotype of the mice during the experiments and initial analyses.

Behavioral testing

Hanging wire test. Mice were brought to a metal wire with a diameter of 2 mm that was suspended approximately 20 cm above a cage, wire so that they could grasp the wire with their front paws. Once a mouse grabbed the wire, the experimenter gently released the mouse and the latency to fall was recorded. The maximal trial duration was 60 s.

Balance beam. Mice were tested on the balance beam as described previously (Wahl et al., 2023). Briefly, the setup consisted of two platforms connected by a metal horizontal beam of 86 cm that was positioned 50 cm above an acrylic glass plate. When reaching the second platform, mice could enter their home cage. On the first training day, mice walk three times on a beam with a diameter of 12 mm and three times on one with a diameter of 10 mm. On the second day, this is repeated, but with diameters of 10, 8, and 6 mm. On the third day, videos are made of three trials on each of the beams, starting with the thickest one.

The recorded crossings on the third day were analyzed on the middle 70 cm of the beams. The crossing time and the number of hindlimb slips were scored, and we noted whether the mice walked or crawled to the other side. Crossings during which the mice fell or jumped off the beam, or when they made a slip severe enough that they could not resume crossing without help from the experimenter, were considered as fails.

ErasmusLadder. Locomotor patterns were recorded on the ErasmusLadder (Noldus, Wageningen, the Netherlands), a horizontal ladder flanked by two plexiglass walls spaced 2 cm apart as described previously (Vinueza Veloz et al., 2015; Haify et al., 2020; Jaarsma et al., 2023). The ladder consists of two rows of 37 rungs spaced 15 mm apart and placed in an alternating high/low pattern. The height difference between high and low rungs is 9 mm. Each rung is connected to a pressure sensor recording rung touch.

During a trial, the mouse had to walk from a shelter box on one side of the ladder to another on the other end. Trial start was indicated by lighting an LED in the shelter box followed three seconds later by a strong tail wind. Early escapes, thus before the LED was switched on, were discouraged by triggering a strong head wind. In between trials, there was a resting period. Mice were first habituated to the setup by letting them freely explore the ladder for 15 min during which no light or air cues were given. On the next day, training started with 42 trials on each day for five consecutive days. Only regular trials, thus trials without pauses or other disruptions, were analyzed as described previously (Jaarsma et al., 2023).

Hildebrand plots (Hildebrand, 1965; Cartmill et al., 2020; Jaarsma et al., 2023) were made to visualize inter-limb coordination. On the x-as, we plotted the fraction of the step cycle during which the right forelimb touched a rung, and on the y-as the fraction of the step cycle between the placement of the right forelimb and a second limb, e.g., the left hindlimb for the diagonal stance. The density of the events was normalized per session, and, for each genotype and stance, we used unsupervised machine learning in combination with *k* means clustering to divide the histograms in two clusters. To this end, we used the pretrained InceptionV3 unsupervised machine learning algorithm from the Keras applications library in Python, whereby we removed the output layer of the pretrained model. The extracted image features were used as input for *k* means clustering ($k = 2$). To control for model sensitivity to the initial conditions, we ran each model ten times and compared the resulting clusters. The difference between the averages of groups 1 ("healthy") and 2 ("affected"), were visualized as heat maps.

Principal component analysis of the ErasmusLadder data was performed on 23 different parameters to perform principal component analysis (PCA), as described previously (Jaarsma et al., 2023). The PCA was performed using the Scikit-learn Python package, with the instruction to retain as much principal components as needed to explain ≥85% of the variance observed.

Three-chamber test for social preference. Mice were placed in a box consisting of three chambers that were accessible by small doors in the two walls. The middle chamber was always empty. The test consists of five steps. In step 1, the mice were placed in the middle chamber for 5 minutes without access to the other chambers in order to habituate to the setup. In the second step (phase 1), all chambers were empty and the baseline preference of the mice was tested for 10 minutes. For step 3 (phase 2), an empty wire mash cup was placed in one of the outer chambers and a cup containing an age and sex matched mouse was placed in the other. The test mouse roamed freely for 10 minutes and preference for time spent with the object (empty cup) or conspecific was calculated (social preference). Step 4 consisted of placing the mouse in the chamber with the cup holding the other mouse for 5 minutes to make sure this mouse is familiar. For step 5 (phase 3), a second age and sex matched mouse was placed under the previously empty cup. During the next 10 minutes, preference for time spent with either the familiar or the novel mouse was calculated.

Marble burying test. Repetitive, obsessive-compulsive behaviour was tested by placing the mice in a large cage with 20 marbles spaced evenly on top of the bedding for 30 minutes. Pictures were taken at 10, 20 and 30 minutes to assess the number of marbles buried. A marble was considered buried if less than 50% of the marble was visible.

Aortic and cardiovascular perfusion and µCT imaging.

Prior to sacrifice, mice were given a sub-lethal i.p. dose of ketamine (100 mg / kg) plus xylazine (6 mg / kg). Vascular perfusions were carried out as described previously (Downey et al., 2012). The abdominal cavity was opened, the diaphragm was incised to expose the pleural cavity, and the ribs were cut away to allow access to the heart. A 25G butterfly needle attached to 0.75 in polyethylene tubing (BD Vacutainer) was inserted into the left ventricle and the right jugular vein severed to provide a drainage point. The circulatory system was flushed with 10 ml of heparinised saline, and this was immediately followed by perfusion with 10 ml of radio-opaque silicone rubber polymer (MicrofilH, MW-122 yellow, Flow-Tech) at a constant rate of 0.75 ml / min using a Harvard Apparatus PHD 2000 Infusion pump (Instech Laboratories Inc). The Microfil compound was allowed to polymerize overnight at 4 °C. Hearts were excised and fixed in 10% neutral buffered formalin (NBF) for a minimum of 24 h prior to µCT scanning. Micro-CT imaging was performed using an ultra-fast µCT scanner (Quantum FX, PerkinElmer). The µCT acquisition parameters were 90 kVp, 160 µA with field of view 20 mm and 360° rotation in 1 step. The acquisition time was 4.5 min. Images in Hounsfield unit (HU) were reconstructed in cubic voxels of 40 µm, generating a matrix of 512 × 512 × 512 voxels. The bones and vascular network were visualized using the volume renderer available from MeVisLab (MeVisLab 2.2.1, MeVis Medical Solutions AG).

Micro-Doppler imaging

Micro-Doppler imaging was used to characterise the brain vasculature. To this end, adult mice (2-3 months old) were measured under isoflurane anaesthesia (initiation: 5% V/V in O_2, maintenance: 1.5-2% V/V in O_2), using 5 mg/kg carprofen (Rimadyl, Pfizer) and lidocaine (Braun) as analgetics.

The µDoppler setup consisted of an ultrasound research system (Vantage 256-LE, Verasonics, Redmond, WA, USA) interfaced with either a high-frequency linear array (L35-16vX, Verasonics, operated at 26.8 MHz, aperture 8.8 mm) for high spatial resolution at the cost of imaging depth, or a lower frequency array (L22-14vX, Verasonics, operated at 15.6 MHz, aperture 12.8 mm) capable of imaging deeper structures with a larger field-of-view. The ultrasound system was coupled to a workstation via a PCIe bridge to allow for fast (6 GB/s) and sustained data transfer. Data processing and Fourier domain image reconstruction was performed on a GPU (Titan GTX 2010, NVIDIA, Santa Clara, CA, USA) using custom-

written C++/CUDA software. The setup was controlled using custom-written LabVIEW software (National Instruments, Austin, TX, USA).

With respect to the ultrasound data acquisition a pulse repetition frequency (determined by the time it takes to acquire the data for one ultrasound image) of 20 kHz was used and 20 angled (between -7 and + 7 degrees) planewaves were averaged for one compounded frame providing a Doppler pulse repetition frequency of 1 kHz. The compounded frames were streamed to disc for further offline processing. For every 2D µDoppler image, a set of 2270 compounded frames was used. Doppler processing consisted of SVD-based clutter filtering (Demené et al., 2015), followed by a 5th order high-pass zero-phase Butterworth filter with a cut-off frequency of 60 Hz. Doppler frames with an average value of one standard deviation below or above the median value for all frames were discarded from the set as they are linked to high overall motion, for example induced by breathing. Spatial upsampling of the Doppler filtered frames to an isotropic grid of 25 µm was performed by zero padding in the frequency domain and the final µDoppler image was obtained by computing the power of the Doppler signal for every pixel. Log compression was applied to compress the visible dynamic range to a level of 25-35 dB depending on the noise-level.

Transthoracic echocardiography.

For echocardiography, mice were shaved and lightly anesthetized with isoflurane (on average 1.5% in oxygen) and allowed to breathe spontaneously via a nasal cone. Non-invasive, echocardiographic parameters were measured using a Vevo®-2100 high frequency ultrasound system (VisualSonics Inc., Toronto, Canada) and analysed using Vevo®-2100-1.6.0 software. Long-axis EKG-triggered cine loops of the left ventricular (LV) contraction cycle were obtained in B-mode to assess end-diastolic/systolic volume. Short-axis recordings of the LV contraction cycle were taken in M-mode to assess wall thickness of the anterior/posterior wall at the mid-papillary level. From B-mode recordings, LV length from basis to apex, LV volumes in systole (LVVs) and diastole (LVVd) were determined. From M-mode recordings, LV posterior wall thickness in systole (LV PWs) and diastole (LV PWd) were determined. LV mass was calculated with the following formula: (0,8*(1.04*(((LVIDd + LV PWd + IVSd)^3)-((LVIDd)^3))+0.6); fractional shortening (FS) was calculated with the following formula: (LVIDd-LVIDs)/LVIDd*100). Ejection fraction (EF) was calculated as ((SV/Vd)*100) with Vs, systolic volume (3.1416*(LVIDs^3)/6), Vd, diastolic volume (3.1416*(LVIDd^3)/6), and SV, stroke volume (Vd-Vs).

Cardiac histological analysis and (immunofluorescence) microscopy.

Prior to histological analysis, hearts were arrested in diastole and perfused with 4% paraformaldehyde (PFA), followed by paraffin embedding and sectioning at 4 µm. These sections were cut and mounted on coated slides and dried overnight at 37C. Slides were dewaxed in xylene and hydrated using graded alcohols to tap water. The sections were subsequently stained with fluorescein isothiocyanate (FITC)-labeled wheat-germ-agglutinin (WGA; Sigma) to visualize and quantify the cell cross-sectional area; hematoxylin and eosin (H&E; Sigma) for routine histological analysis; and Sirius Red (Sigma) for detection of fibrillar collagen. For immunofluorescence, sections were dried, fixed with 4% PFA, and permeabilized with 0.1% Triton X-100 (Sigma), dissolved in 1% BSA in PBS for 10 min and blocked with 10% goat serum in PBS for 60 min. Then, the slides were incubated overnight with primary antibody diluted in 0.1% BSA in PBS at 4 °C. Secondary antibody incubation was performed at room temperature for 1 h, followed by 5 min Hoechst incubation and mounting with Fluoromount (Southern Biotech). Images were taken using an Olympus BX63 microscope and analyzed in ImageJ.

Brain histological analysis

For the visualization of blood vessels in the brain, we used adult (>3 months) mice. Mice were anesthetized with pentobarbital (80 mg/kg i.p.) and transcardially perfused first with 4% paraformaldehyde and then with 10% Indian ink mixed with 2% gelatin (preheated to 40 °C), based on a previously published method (Xue et al., 2014). After injection of the ink, the mice were placed with their ventral side up for 10-20 min at -20 °C to solidify the gelatin. Afterwards, the brains were extracted, fixed for 2 h in 4% paraformaldehyde, and incubated overnight in 0.1 M phosphate buffer (PB)

with 10% sucrose at 4 °C. Next, the brains were embedded in 14% gelatin/10% sucrose and postfixed for 2 h in 10% formaldehyde/30% sucrose. After another overnight incubation, this time in 0.1 M PB with 30% sucrose, 40 µm sagittal sections were cut on a sliding microtome while being cooled with dry ice. The sections were processed freely floating, washed twice with 0.1 M phosphate-buffered saline (PBS), blocked for endogenous peroxidase activity (1% H_2O_2 in 0.1 M PBS), washed again twice in PBS, and were stained for 3 minutes in a 1 % thionine solution, followed by a differentiation of the sections in 96% ethanol, followed by dehydration using several steps with 100% ethanol and xylene, and cover slipped with Permount mounting medium (Fisher Scientific, Waltham, MA, USA).

In the section approx. 100 µm lateral of the midline, areas of 650x750 µm were chosen for counting the number of loops under a light microscope. For each mouse, we counted the loops in the hippocampus, cerebellar cortex and brainstem. The total number of loops per brain region, per mouse was reported.

From these same sections, binary images of the cerebral cortex were made in ImageJ, selecting only those pixels that contained stained blood vessels. The binary image was skeletonized using the AnalyzeSkeleton plugin (Arganda-Carreras et al., 2010). The skeleton was subsequently used for fractal dimension analysis with the FracLac plugin (http://rsb.info.nih.gov/ij/plugins/fraclac/FLHelp/Introduction.htm), as well as for skeletal analysis in MATLAB. Here, the binarized images were split into line-segments using the bwmorph function from the Image Processing Toolbox, so that each blood vessel segment could be analyzed independently. For each blood vessel segment the tortuosity (i.e., ratio between the length of the curve and the distance between its end points) was calculated. The tortuosity is 1 for a straight-line segment and increases the further the vessel deviates from the straight-line path.

Statistical analysis. The results are presented as mean ± standard error of the mean (s.e.m.), unless stated otherwise. All statistical analyses were performed with Prism software (GraphPad Software). ANOVA test followed by Tukey's post-test when group differences were detected at the 5% significance level, or Student's t-test were performed to compare two experimental groups, unless stated otherwise. Differences were considered significant when $P<0.05$.

Acknowledgments
Financial support for this study was provided by Health Holland to promote public private partnerships (TKI-LSH EMCLSH21017; L.W.J.B.) ZonMw Veni (91619109; L.K.), Erasmus Medical Center Fellowship (L.K.), the Medical Delta Programme (L.K. & C.I.D.Z) and LSH-NWO Crossover (INTENSE; L.K. & C.I.D.Z.). This publication is part of the project CUBE (with project number 108845) of the research programme NWO-Groot which is partly financed by the Dutch Research Council (NWO; B.S.G., S.K.E.K., P.K., C.I.D.Z.).

Name	Designed research	Performed research	Contributed new analytic tools	Analyzed data	Wrote the paper (with contributions from all authors)
Hamid el-Azzouzi	x	x	x	x	x
Laurens Bosman	x	x	x	x	x
Lieke Kros	x	x		x	
Nicole van Vliet		x		x	
Yanto Ridwan		x		x	
Stéphanie Dijkhuizen	x	x		x	
Erika Sabel-Goednegt	x	x		x	
Bastian Generowicz			x	x	
Manuele Novello				x	
Emma Kretschmann				x	
Morrisen Snoeren				x	
Danique Broere		x		x	
Rocco Caliandro					
Sebastiaan Koekkoek			x		
Pieter Kruizinga			x	x	
Vera van Dis	x			x	
Haibo Zhou	x	x			
Hui Yang	x	x			
Changyang Zhou	x	x			
Ingrid van der Pluijm	x				
Jeroen Essers	x			x	
Chris De Zeeuw	x		x	x	

References

Akimoto T, Suenaga J, Hayashi T, Hirokawa D, Ito S, Sato H, Yamamoto T (2022) Moyamoya syndrome in a patient with Williams syndrome: A case report. Pediatr Neurosurg 57:365-370.

Arganda-Carreras I, Fernández-González R, Muñoz-Barrutia A, Ortiz-De-Solorzano C (2010) 3D reconstruction of histological sections: Application to mammary gland tissue. Microsc Res Tech 73:1019-1029.

Barozzi S, Soi D, Gagliardi C, Selicorni A, Bedeschi MF, Forti S, Di Berardino F, Cesarani A, Brambilla D (2013) Balance function in patients with Williams syndrome. Gait & posture 38:221-225.

Bayés M, Magano LF, Rivera N, Flores R, Pérez Jurado LA (2003) Mutational mechanisms of Williams-Beuren syndrome deletions. Am J Hum Genet 73:131-151.

Belknap JK, Grieshaber NA, Schwartz PE, Orton EC, Reidy MA, Majack RA (1996) Tropoelastin gene expression in individual vascular smooth muscle cells. Relationship to DNA synthesis during vascular development and after arterial injury. Circ Res 78:388-394.

Bellugi U, Bihrle A, Jernigan T, Trauner D, Doherty S (1990) Neuropsychological, neurological, and neuroanatomical profile of Williams syndrome. Am J Med Genet Suppl 6:115-125.

Beuren AJ, Apitz J, Harmjanz D (1962) Supravalvular aortic stenosis in association with mental retardation and a certain facial appearance. Circulation 26:1235-1240.

Borralleras C, Sahun I, Perez-Jurado LA, Campuzano V (2015) Intracisternal *Gtf2i* gene therapy ameliorates deficits in cognition and synaptic plasticity of a mouse model of Williams-Beuren Syndrome. Mol Ther 23:1691-1699.

Bozlak S, Uludağ Alkaya D, Kasap B, Yüksel Ülker A, Yildiz CA, Altindağ V, Ülkersoy I, Çifçi Sunamak E, Dedeoğlu R, Tüysüz B (2023) A large Turkish cohort of Williams syndrome: The evaluation of facial, cardiovascular, and neuropsychiatric features. Turk Arch Pediatr 58:182-188.

Brar JS, Verma R, Al-Omari M, Siu VM, Andrade AV, Jurkiewicz MT, Lalgudi Ganesan S (2022) Moyamoya syndrome in an infant with Aicardi-Goutieres and Williams syndromes: A case report. Neuropediatrics 53:204-207.

Bräuninger H, Krüger S, Bacmeister L, Nyström A, Eyerich K, Westermann D, Lindner D (2023) Matrix metalloproteinases in coronary artery disease and myocardial infarction. Basic Res Cardiol 118:18.

Brkic M, Balusu S, Libert C, Vandenbroucke RE (2015) Friends or foes: Matrix metalloproteinases and their multifaceted roles in neurodegenerative diseases. Mediators Inflamm 2015:620581.

Cartmill M, Brown K, Atkinson C, Cartmill EA, Findley E, Gonzalez-Socoloske D, Hartstone-Rose A, Mueller J (2020) The gaits of marsupials and the evolution of diagonal-sequence walking in primates. American journal of physical anthropology 171:182-197.

Chapman SL, Sicot FX, Davis EC, Huang J, Sasaki T, Chu ML, Yanagisawa H (2010) Fibulin-2 and fibulin-5 cooperatively function to form the internal elastic lamina and protect from vascular injury. Arterioscler Thromb Vasc Biol 30:68-74.

Cocciolone AJ, Hawes JZ, Staiculescu MC, Johnson EO, Murshed M, Wagenseil JE (2018) Elastin, arterial mechanics, and cardiovascular disease. Am J Physiol Heart Circ Physiol 315:H189-H205.

Collins RT, 2nd, Kaplan P, Somes GW, Rome JJ (2010) Long-term outcomes of patients with cardiovascular abnormalities and Williams syndrome. Am J Cardiol 105:874-878.

Currie S, Raghavan A, Batty R, Connolly DJ, Griffiths PD (2011) Childhood moyamoya disease and moyamoya syndrome: a pictorial review. Pediatr Neurol 44:401-413.

Del Campo M, Antonell A, Magano LF, Muñoz FJ, Flores R, Bayés M, Pérez Jurado LA (2006) Hemizygosity at the *NCF1* gene in patients with Williams-Beuren syndrome decreases their risk of hypertension. Am J Hum Genet 78:533-542.

Demené C, Deffieux T, Pernot M, Osmanski BF, Biran V, Gennisson JL, Sieu LA, Bergel A, Franqui S, Correas JM, Cohen I, Baud O, Tanter M (2015) Spatiotemporal clutter filtering of ultrafast ultrasound data highly increases Doppler and fUltrasound sensitivity. IEEE Trans Med Imaging 34:2271-2285.

DeSilva U, Elnitski L, Idol JR, Doyle JL, Gan W, Thomas JW, Schwartz S, Dietrich NL, Beckstrom-Sternberg SM, McDowell JC, Blakesley RW, Bouffard GG, Thomas PJ, Touchman JW, Miller W, Green ED (2002) Generation and comparative analysis of approximately 3.3 Mb of mouse genomic sequence orthologous to the region of human chromosome 7q11.23 implicated in Williams syndrome. Genome Res 12:3-15.

Dietz HC, Mecham RP (2000) Mouse models of genetic diseases resulting from mutations in elastic fiber proteins. Matrix Biol 19:481-488.

Downey CM, Singla AK, Villemaire ML, Buie HR, Boyd SK, Jirik FR (2012) Quantitative ex-vivo micro-computed tomographic imaging of blood vessels and necrotic regions within tumors. PLoS One 7:e41685.

Doyle TF, Bellugi U, Korenberg JR, Graham J (2004) "Everybody in the world is my friend" hypersociability in young children with Williams syndrome. American journal of medical genetics Part A 124A:263-273.

Ewart AK, Morris CA, Atkinson D, Jin W, Sternes K, Spallone P, Stock AD, Leppert M, Keating MT (1993) Hemizygosity at the elastin locus in a developmental disorder, Williams syndrome. Nat Genet 5:11-16.

Fukui M (1997) Guidelines for the diagnosis and treatment of spontaneous occlusion of the circle of Willis ('moyamoya' disease). Research Committee on Spontaneous Occlusion of the Circle of Willis (Moyamoya Disease) of the Ministry of Health and Welfare, Japan. Clin Neurol Neurosurg 99 Suppl 2:S238-240.

Fusco C, Micale L, Augello B, Teresa Pellico M, Menghini D, Alfieri P, Cristina Digilio M, Mandriani B, Carella M, Palumbo O, Vicari S, Merla G (2014) Smaller and larger deletions of the Williams Beuren syndrome region implicate genes involved in mild facial phenotype, epilepsy and autistic traits. Eur J Hum Genet 22:64-70.

Gagliardi C, Martelli S, Burt MD, Borgatti R (2007) Evolution of neurologic features in Williams syndrome. Pediatr Neurol 36:301-306.

Haify SN, Mankoe RSD, Boumeester V, van der Toorn EC, Verhagen RFM, Willemsen R, Hukema RK, Bosman LWJ (2020) Lack of a clear behavioral phenotype in an inducible FXTAS mouse model despite the presence of neuronal FMRpolyG-positive aggregates. Front Mol Biosci 7:599101.

Hammond P, Hutton TJ, Allanson JE, Buxton B, Campbell LE, Clayton-Smith J, Donnai D, Karmiloff-Smith A, Metcalfe K, Murphy KC, Patton M, Pober B, Prescott K, Scambler P, Shaw A, Smith AC, Stevens AF, Temple IK, Hennekam R, Tassabehji M (2005) Discriminating power of localized three-dimensional facial morphology. Am J Hum Genet 77:999-1010.

Hawes JZ, Cocciolone AJ, Cui AH, Griffin DB, Staiculescu MC, Mecham RP, Wagenseil JE (2020) Elastin haploinsufficiency in mice has divergent effects on arterial remodeling with aging depending on sex. Am J Physiol Heart Circ Physiol 319:H1398-H1408.

Hildebrand M (1965) Symmetrical gaits of horses. Science 150:701-708.

Hobart HH, Morris CA, Mervis CB, Pani AM, Kistler DJ, Rios CM, Kimberley KW, Gregg RG, Bray-Ward P (2010) Inversion of the Williams syndrome region is a common polymorphism found more frequently in parents of children with Williams syndrome. Am J Med Genet C Semin Med Genet 154C:220-228.

Hoogenraad CC, Akhmanova A, Galjart N, De Zeeuw CI (2004) LIMK1 and CLIP-115: linking cytoskeletal defects to Williams syndrome. Bioessays 26:141-150.

Hoogenraad CC, Eussen BHJ, Langeveld A, van Haperen R, Winterberg S, Wouters CH, Grosveld F, De Zeeuw CI, Galjart N (1998) The murine *CYLN2* gene: genomic organization, chromosome localization, and comparison to the human gene that is located within the 7q11.23 Williams syndrome critical region. Genomics 53:348-358.

Hoogenraad CC, Koekkoek B, Akhmanova A, Krugers H, Dortland B, Miedema M, van Alphen A, Kistler WM, Jaegle M, Koutsourakis M, Van Camp N, Verhoye M, van der Linden A, Kaverina I, Grosveld F, De Zeeuw CI, Galjart N (2002) Targeted mutation of *Cyln2* in the Williams syndrome critical region links CLIP-115 haploinsufficiency to neurodevelopmental abnormalities in mice. Nat Genet 32:116-127.

Howald C, Merla G, Digilio MC, Amenta S, Lyle R, Deutsch S, Choudhury U, Bottani A, Antonarakis SE, Fryssira H, Dallapiccola B, Reymond A (2006) Two high throughput technologies to detect segmental aneuploidies identify new Williams-Beuren syndrome patients with atypical deletions. J Med Genet 43:266-273.

Hutchinson KR, Stewart JA, Jr., Lucchesi PA (2010) Extracellular matrix remodeling during the progression of volume overload-induced heart failure. J Mol Cell Cardiol 48:564-569.

Ito Y, Ito T, Kurahashi N, Ochi N, Noritake K, Sugiura H, Mizuno S, Kidokoro H, Natsume J, Nakamura M (2020) Gait characteristics of children with Williams syndrome with impaired visuospatial recognition: a three-dimensional gait analysis study. Exp Brain Res 238:2887-2895.

Jaarsma D, Birkisdóttir MB, van Vossen R, Oomen DWGD, Akhiyat O, Vermeij WP, Koekkoek SKE, De Zeeuw CI, Bosman LWJ (2023) Different Purkinje cell pathologies cause specific patterns of progressive ataxia in mice. bioRxiv:2023.2008.2029.555378.

Kawai M, Nishikawa T, Tanaka M, Ando A, Kasajima T, Higa T, Tanikawa T, Kagawa M, Momma K (1993) An autopsied case of Williams syndrome complicated by moyamoya disease. Acta Paediatr Jpn 35:63-67.

Kopp N, McCullough K, Maloney SE, Dougherty JD (2019) *Gtf2i* and *Gtf2ird1* mutation do not account for the full phenotypic effect of the Williams syndrome critical region in mouse models. Hum Mol Genet 28:3443-3465.

Kozel BA, Barak B, Kim CA, Mervis CB, Osborne LR, Porter M, Pober BR (2021) Williams syndrome. Nat Rev Dis Primers 7:42.

Leonova EI, Gainetdinov RR (2020) CRISPR/Cas9 Technology in Translational Biomedicine. Cell Physiol Biochem 54:354-370.

Li HH, Roy M, Kuscuoglu U, Spencer CM, Halm B, Harrison KC, Bayle JH, Splendore A, Ding F, Meltzer LA, Wright E, Paylor R, Deisseroth K, Francke U (2009) Induced chromosome deletions cause hypersociability and other features of Williams-Beuren syndrome in mice. EMBO Mol Med 1:50-65.

Liu H, Mo ZH, Yang H, Zhang ZF, Hong D, Wen L, Lin MY, Zheng YY, Zhang ZW, Xu XW, Zhuang J, Wang SS (2021) Automatic facial recognition of Williams-Beuren Syndrome based on deep convolutional neural networks. Front Pediatr 9:648255.

Lugo M, Wong ZC, Billington CJ, Jr., Parrish PCR, Muldoon G, Liu D, Pober BR, Kozel BA (2020) Social, neurodevelopmental, endocrine, and head size differences associated with atypical deletions in Williams-Beuren syndrome. American journal of medical genetics Part A 182:1008-1020.

Meyer-Lindenberg A, Hariri AR, Munoz KE, Mervis CB, Mattay VS, Morris CA, Berman KF (2005) Neural correlates of genetically abnormal social cognition in Williams syndrome. Nat Neurosci 8:991-993.

Ortiz-Romero P, González-Simón A, Egea G, Pérez-Jurado LA, Campuzano V (2021) Co-treatment with verapamil and curcumin attenuates the behavioral alterations observed in Williams-Beuren Syndrome mice by regulation of MAPK pathway and microglia overexpression. Front Pharmacol 12:670785.

Parrish PCR, Liu D, Knutsen RH, Billington CJ, Mecham RP, Fu YP, Kozel BA (2020) Whole exome sequencing in patients with Williams-Beuren syndrome followed by disease modeling in mice points to four novel pathways that may modify stenosis risk. Hum Mol Genet 29:2035-2050.

Peoples R, Franke Y, Wang YK, Pérez-Jurado L, Paperna T, Cisco M, Francke U (2000) A physical map, including a BAC/PAC clone contig, of the Williams-Beuren syndrome--deletion region at 7q11.23. Am J Hum Genet 66:47-68.

Pérez Jurado LA, Peoples R, Kaplan P, Hamel BCJ, Francke U (1996) Molecular definition of the chromosome 7 deletion in Williams syndrome and parent-of-origin effects on growth. Am J Hum Genet 59:781-792.

Pober BR (2010) Williams-Beuren syndrome. N Engl J Med 362:239-252.

Segura-Puimedon M, Sahún I, Velot E, Dubus P, Borralleras C, Rodrigues AJ, Valero MC, Valverde O, Sousa N, Herault Y, Dierssen M, Pérez-Jurado LA, Campuzano V (2014) Heterozygous deletion of the Williams-Beuren syndrome critical interval in mice recapitulates most features of the human disorder. Hum Mol Genet 23:6481-6494.

Sentmanat MF, Peters ST, Florian CP, Connelly JP, Pruett-Miller SM (2018) A Survey of Validation Strategies for CRISPR-Cas9 Editing. Sci Rep 8:888.

Soper R, Chaloupka JC, Fayad PB, Greally JM, Shaywitz BA, Awad IA, Pober BR (1995) Ischemic stroke and intracranial multifocal cerebral arteriopathy in Williams syndrome. J Pediatr 126:945-948.

Tassabehji M, Metcalfe K, Karmiloff-Smith A, Carette MJ, Grant J, Dennis N, Reardon W, Splitt M, Read AP, Donnai D (1999) Williams syndrome: use of chromosomal microdeletions as a tool to dissect cognitive and physical phenotypes. Am J Hum Genet 64:118-125.

Terashita S, Nakaoka H, Ibuki K, Ozawa S, Hirono K, Adachi Y, Fujita S, Nakanishi T, Ichida F (2019) Only characteristics vascular lesions of Williams-Beuren syndrome in a girl with a novel nonsense *ELN* mutation. J Pediatr Cardiol Card Surg 3:56-60.

Thomson J, Singh M, Eckersley A, Cain SA, Sherratt MJ, Baldock C (2019) Fibrillin microfibrils and elastic fibre proteins: Functional interactions and extracellular regulation of growth factors. Semin Cell Dev Biol 89:109-117.

Tomc SA, Williamson NK, Pauli RM (1990) Temperament in Williams syndrome. Am J Med Genet 36:345-352.

Tonelli AR, Ahmed M, Hamed F, Prieto LR (2015) Peripheral pulmonary artery stenosis as a cause of pulmonary hypertension in adults. Pulm Circ 5:204-210.

Urbán Z, Michels VV, Thibodeau SN, Davis EC, Bonnefont JP, Munnich A, Eyskens B, Gewillig M, Devriendt K, Boyd CD (2000) Isolated supravalvular aortic stenosis: functional haploinsufficiency of the elastin gene as a result of nonsense-mediated decay. Hum Genet 106:577-588.

van der Geest JN, Lagers-van Haselen GC, van Hagen JM, Govaerts LCP, de Coo IFM, de Zeeuw CI, Frens MA (2004) Saccade dysmetria in Williams-Beuren syndrome. Neuropsychologia 42:569-576.

van Hagen JM, van der Geest JN, van der Giessen RS, Lagers-van Haselen GC, Eussen HJFMM, Gille JJP, Govaerts LCP, Wouters CH, de Coo IFM, Hoogenraad CC, Koekkoek SKE, Frens MA, van Camp N, van der Linden A, Jansweijer MCE, Thorgeirsson SS, De Zeeuw CI (2007) Contribution of CYLN2 and GTF2IRD1 to neurological and cognitive symptoms in Williams Syndrome. Neurobiol Dis 26:112-124.

Vinueza Veloz MF, Zhou K, Bosman LWJ, Potters JW, Negrello M, Seepers RM, Strydis C, Koekkoek SKE, De Zeeuw CI (2015) Cerebellar control of gait and interlimb coordination. Brain structure & function 220:3513-3536.

Wågsäter D, Zhu C, Bjorkegren J, Skogsberg J, Eriksson P (2011) MMP-2 and MMP-9 are prominent matrix metalloproteinases during atherosclerosis development in the *Ldlr*$^{-/-}$*Apob*$^{100/100}$ mouse. Int J Mol Med 28:247-253.

Wahl L, Kaiser FMP, Bentvelzen M, White J, Schonewille M, Badura A (2023) Detecting ataxia using an automated analysis of motor coordination and balance of mice on the balance beam. bioRxiv:2023.2007.2003.547476.

Williams JC, Barratt-Boyes BG, Lowe JB (1961) Supravalvular aortic stenosis. Circulation 24:1311-1318.

Wint DP, Butman JA, Masdeu JC, Meyer-Lindenberg A, Mervis CB, Sarpal D, Morris CA, Berman KF (2014) Intracranial arteries in individuals with the elastin gene hemideletion of Williams syndrome. AJNR Am J Neuroradiol 35:90-94.

Wollack JB, Kaifer M, LaMonte MP, Rothman M (1996) Stroke in Williams syndrome. Stroke 27:143-146.
Xue S, Gong H, Jiang T, Luo W, Meng Y, Liu Q, Chen S, Li A (2014) Indian-ink perfusion based method for reconstructing continuous vascular networks in whole mouse brain. PLoS One 9:e88067.
Yanagisawa H, Schluterman MK, Brekken RA (2009) Fibulin-5, an integrin-binding matricellular protein: its function in development and disease. J Cell Commun Signal 3:337-347.
Zhou J, Wu Y, Xu X, Zhang Y, Zhang X, Chen H, Zhuang J, Chen J, Teng Y (2022) Identification and characterization of novel elastin gene mutations in eleven families with supravalvular aortic stenosis. Front Genet 13:1059640.